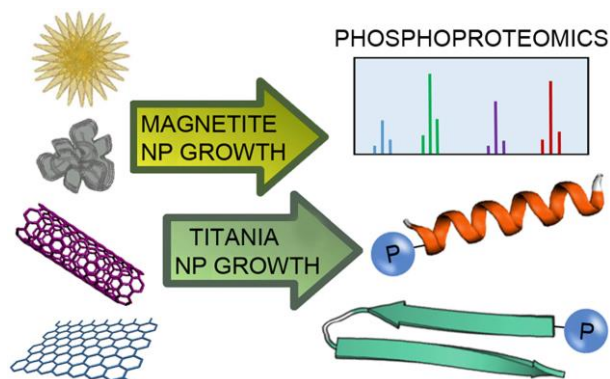


TABLE OF CONTENTS (TOC)



Nanocomposites are prepared from different carbon nanostructure scaffolds for magnetite and titania nanoparticle nucleation and growth. Their performance surpasses the commercial reference in NanoHPLC-MS/MS analysis of cancer cell lysates for phosphopeptide enrichment and detection.

Carbon Nanostructure Morphology Templates Nanocomposites for Phosphoproteomics

Susy Piovesana¹, Daniel Iglesias², Manuel Melle-Franco³, Slavko Kralj⁴, Chiara Cavaliere¹, Michele Melchionna², Aldo Laganà^{1,5} Anna L. Capriotti¹ (✉), and Silvia Marchesan² (✉)

¹ Piazzale A. Moro 5, Dipartimento di Chimica, Sapienza Università di Roma, Rome 00185, Italy

² Via L. Giorgieri 1, Dipartimento di Scienze Chimiche e Farmaceutiche, Università di Trieste, Trieste 34127, Italy

³ CICECO, University of Aveiro, Aveiro 3810-193, Portugal

⁴ Jamova 39, Department for Materials Synthesis, Jožef Stefan Institute, Ljubljana 1000, Slovenia

⁵ Via Monteroni Campus Ecotekne, CNR NANOTEC, University of Salento, Lecce 73100, Italy

ABSTRACT

Protein and peptide phosphorylation regulate numerous pathological processes, however, their characterization is challenging due to their low abundance and transient nature. Therefore, nanomaterials are being developed to address this demanding task. In particular, carbon nanostructures are attracting interest as scaffolds for functional nanocomposites, yet only isolated studies exist on the topic, and little is known on the effect of nanocarbon morphology on templating nanocomposites. In this work, we compared oxidized carbon nanotubes, graphene oxide, oxidized carbon nanohorns and oxidized graphitized carbon black, as scaffolds for magnetized nanocomposites. The nanomaterials were extensively characterized with experimental and *in silico* techniques. Next, they were applied to phosphopeptide enrichment from cancer cell lysates for NanoHPLC-MS/MS, with selectivity as high as nearly 90% and several-thousand identification hits. Overall, new insights emerged for the understanding and the design of nanocomposites for phosphoproteomics.

KEYWORDS

Nanocomposites, carbon nanotubes, graphene oxide, carbon nanohorns, carbon, titania, proteomics.

Introduction

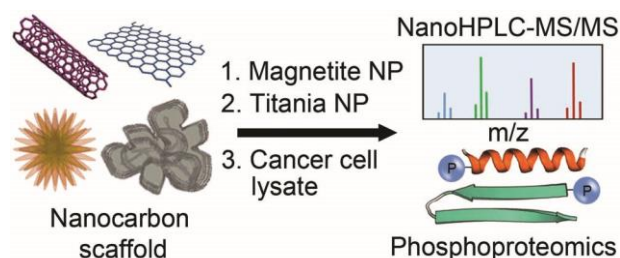
Nanomaterials' high surface-to-volume ratio and easy functionalization are attractive features for diverse uses, with carbon nanostructures being convenient scaffolds to obtain functional composites or hybrid materials [1, 2]. Their peculiar properties can be fine-tuned by derivatization, be it covalent and/or non-covalent, with electrostatic and π - π interactions being widely adopted choices [3-6]. In particular, their interface with nanostructured titania is the focus of numerous investigations, mainly within the area of catalysis [7-11]. What is less known is that nanostructured titania can be advantageous for phosphoproteomics, thanks to its high surface area and binding of phosphorylated peptides that allow their enrichment to facilitate their detection [12]. The characterization of proteins' and peptides' phosphorylation state in a biological sample provides precious information about physiological and pathological conditions, because this rapid modification is a universal switch in a plethora of biological pathways. Addition and removal of phosphate groups offers the means to regulate cellular functions, and it is altered in disease processes [13]. Unfortunately, phosphorylated forms of biomolecules are transient, thus their characterization constitutes a key analytical challenge in shotgun proteomics analysis, especially of complex samples [14-16].

Amongst the different strategies that have been devised to address this issue, effective approaches consist of immobilized metal ion affinity chromatography (IMAC) and metal oxide affinity chromatography (MOAC) [17]. The use of TiO₂ as material for phosphopeptide enrichment in phosphoproteomics analytical workflows belongs to the MOAC strategy and it is based on the ability of TiO₂ to create coordination complexes with the phosphate groups [18]. Both methods nowadays yield excellent performances in shotgun phosphopeptide analysis, even though a universal strategy to enrich biomolecules is still missing, for which new materials are continuously being searched as useful phases [19]. In particular, nanostructures have attracted great attention, especially to isolate the target analytes from the sample, and to enhance their relative abundance for mass spectrometric detection [20-23].

In this regard, carbon-based (nano)composites coupled to a MOAC strategy avoid common pitfalls, such as aggregation of MO nanoparticles (NPs), while adding the advantageous increased contact between the target biomolecule and the affinity material. Carbon nanotubes (CNTs) [24] and graphene (G) or its derivatives [25, 26] have been used in isolated reports, and it appears evident that research interest will encompass new carbon nanomaterials as soon as they get discovered, and new morphological effects are described [27-29]. However, to our knowledge, other carbon nanostructures, such as carbon nanohorns (CNHs), have not yet been investigated for this application. CNHs consist of horn-shaped clusters of single-walled graphitic cones that display bud-like or dahlia-like morphology and an overall diameter of 50-100 nm [5, 30]. There is ample scope for their use, for instance it was shown they have an ideal porosity to surpass both CNTs and G in catalytic applications, thus they are attractive candidates to be tested for functional composites [31]. Unfortunately, to date, there is no comprehensive study on the morphological effects of different carbon nanostructures as they interface other components in nanocomposites and on their performance for phosphoproteomics. Therefore, CNTs, GO and CNHs were chosen for this study as models of graphitic templates for the nucleation and growth of metal oxides to yield nanocomposites. GCB was also included because it is somewhat more applied in the analytical field as it is known to be capable of extracting neutral, basic, and acidic compounds [32, 33]. This property arises from the graphitic structure that allows van der Waals interactions, as well as the surface functionalization produced by the chemisorption of oxygen, and that favors anion-exchange [34]. Clearly, oxidized graphitic structures could

be suitable scaffolds for the preparation of nanocomposites for phosphopeptide enrichment, thus they were chosen as the starting point for this study [35, 36].

We figured that magnetization would allow convenient magnetic separation of the solid-phase for NanoHPLC-MS/MS analysis [37], while titania NP nucleation and growth could be affected by the nanocarbon scaffold in unexpected ways, constituting an interesting parameter for appropriate interaction with phosphopeptides. The resulting composites were applied for the enrichment of these biomolecules in a complex real matrix (Scheme 1), *i.e.*, HeLa cancer cell lysates, and compared against a titania-based commercial product, to fully understand the differences in enrichment capability. The enrichment protocol was embedded within a typical shotgun proteomics workflow – a realistic application – and revealed a performance with phosphopeptide selectivity as high as nearly 90% and several-thousand identification hits.



Scheme 1 Nanocomposite preparation and application in phosphoproteomics. Each nanocarbon scaffold is used as template for magnetite (1) and titania (2) nanoparticle (NP) nucleation and growth. Each nanocomposite is applied to cancer cell lysates (3) to enrich phosphopeptides for NanoHPLC-MS/MS analysis.

1. Experimental Procedures

1.1 Materials and Methods

All chemicals, including GCB Supelclean ENVI-Carb, reagents, protein standards and solvents were purchased from Sigma-Aldrich (St. Louis, MO, USA) unless stated otherwise. Promega (Madison, WI, USA) supplied trypsin/lys-C Mix of Mass Spec Grade. MilliQ water was prepared using a Sartorius (Göttingen, Germany) system consisting of arium 611 VF. Multi-walled CNTs and exfoliated G were kindly provided by Thomas Swan Co. Ltd. (UK). Carbonium s.r.l. (Italy) kindly supplied CNHs. Transmission electron microscopy (TEM) micrographs were acquired with a Philips EM 208 with a 100 keV acceleration voltage and using a standard loop filament, and a Olympus Morada 2K x 2K CCD camera. Samples were dispersed in methanol and dropcasted on a 300-mesh carbon grid (copper). Prior to TEM analysis, residual solvent was evaporated *in vacuo*. Thermogravimetric analysis (TGA) was performed using a TA TGA Q500 either under air or nitrogen gas as specified, with a flow of 90 ml min⁻¹, and with a temperature range of 100-800 °C and a heating ramp of 10 °C/min. TGA experiments were performed in duplicates. Fourier transform infrared spectroscopy (FT-IR) spectra were acquired from 4000 to 400 cm⁻¹ using a PerkinElmer 2000 instrument, and pellets that were obtained by pressing a mixture of the corresponding sample with anhydrous KBr. Raman spectra were acquired on a Renishaw Invia reflex spectrophotometer with 532 laser (22.5 W). Raman spectra were recorded on several points across each samples, averaged, and then normalized relative to the G band. Porosimetry data was obtained using a 3Flex Surface Characterization Analyzer (Micromeritics Instrument Corporation, Norcross, GA, U.S.A.). Zeta potential was measured for dispersions of the composite materials at 1 mg mL⁻¹ in milliQ water by using a Zetasizer Nano ZS (Malvern, Herrenberg, Germany) equipped with a 633 nm He-Ne laser and operating at an angle of 173°. The sample (10 µL) was placed in a ZEN0040 cuvette (Malvern, Herrenberg, Germany) and the measurements performed at fixed position (4.65 mm) with an automatic attenuator and at a controlled temperature as reported previously [38]. The zeta potential was calculated from the electrophoretic mobility by means of the Henry

correction to Smoluchowski's equation. Data analysis was performed averaging three measurements by Malvern Zetasizer software with Zetasizer Nano ZS (Malvern, Herrenberg, Germany). Magnetic properties were determined at room temperature on a LakeShore 7400 Series vibrating-sample magnetometer (VSM). The XRD measurements were performed with a Xeuss 2.0 Q-Xoom system (Xenocs SA, Sassenage, France), equipped with a micro-focus Genix 3D X-ray Cu source ($\lambda = 0.1542$ nm), a two-dimensional Pilatus3 R 300K detector placed at a distance of 23.6 cm, and an additional Pilatus3 R 100K detector at fixed shorter distance from the sample (14 cm) and tilted at 36 degrees to access larger scattering angles (Dectris Ltd., Baden, Switzerland). Calibration of the sample-detector distance was performed using silver behenate for the small-angle region and Al_2O_3 for the fixed-distance wide-angle detector. Sample powders were loaded into 0.5-mm thick washers used as spacers, closed with sticky Kapton windows and placed in the instrument sample chamber at reduced pressure (~ 0.2 mbar). The beam size was defined to be 0.8 mm \times 0.8 mm. The two-dimensional scattering patterns were subtracted for the "dark" counts, and then masked, azimuthally averaged and normalized for transmitted beam intensity, exposure time and subtended solid angle per pixel, by using the FoxTrot software developed at SOLEIL. The one-dimensional I vs. 2θ profiles were obtained merging data from the detectors (after subtraction for the contributions of the empty polymeric windows) and then put in absolute scale units (cm^{-1}) by dividing for the nominal sample thickness 0.05 cm.

1.2 Carbon nanostructure oxidation

For CNT oxidation, in a round-bottom flask, concentrated nitric acid (69 %, 4 ml) and sulfuric acid (95 %, 12 ml) were mixed together and this was followed by the addition of pristine CNTs (100 mg), and sonication in a Branson ultrasound sonic bath at room temperature for 5 h. The mixture was then cooled down and slowly added to ice-cold water (200 mL). The reaction crude was filtered through Millipore membrane (JHWP, 0.45 μm) and washed with deionized water until the washings reached a neutral pH, then it was washed with methanol and dried with diethyl ether to yield approximately 98 mg of oxidized CNTs.

For CNH oxidation, a round-bottom flask containing pristine CNHs (100 mg) and concentrated nitric acid (69 %, 100 ml) was placed in a Branson ultrasonic bath, and sonicated at 35 $^\circ\text{C}$ for 3 h. The mixture was then gently added to ice-cold water (200 mL) and the crude was filtered through a Millipore membrane (JHWP, 0.45 μm) and washed first with deionized water until a neutral pH was reached, and then with methanol. The black powder was neutralization of the washings. The black powder was dried with diethyl ether to afford approximately 99 mg of CNHs.

To prepare GO, Graphene (G, 200 mg) was added to a 100-ml round-bottom flask that contained $\text{K}_2\text{S}_2\text{O}_8$ (200 mg, 0.37 mmol), P_2O_5 (100 mg, 0.35 mmol) and sulfuric acid (10 ml). The reaction mixture was stirred for 4 hours at 80 $^\circ\text{C}$. The reaction crude was then cooled down, and slowly added to ice-cold deionized water (50 ml). The mixture was then filtered through a Millipore membrane (JHWP, 0.45 μm). Washings were performed with deionized water until a neutral pH was reached. The black powder was next transferred into a round-bottom flask, whereby at 0 $^\circ\text{C}$ the addition of KMnO_4 (100 mg, 0.63 mmol) and H_2SO_4 (20 ml) was performed, followed by stirring for 2 hours at 35 $^\circ\text{C}$. This step was followed by the addition of deionized water (20 ml) and H_2O_2 30 % (2.4 ml) and further stirring for another 15 min. Next, the reaction mixture was filtered using a Millipore membrane (JHWP, 0.45 μm). Washings were performed first with HCl 1 M (100 ml), and then with deionized water until a neutral pH was reached. Further washings were performed with methanol and the black powder was dried with diethyl ether to yield 216 mg of GO.

For GCB oxidation, 6 ml of H_2SO_4 (95 %) and 2 ml of HNO_3 (69%) were mixed in a round-bottom flask. GCB (100 mg) was added on top and the mixture stirred at 80 $^\circ\text{C}$ for 7 h. Once the reaction cooled down, the mixture was slowly added to ice-cold deionized water (200 mL). The crude was filtered through Millipore membrane (JHWP, 0.45 μm), washed with deionized water until the washings reached a neutral pH. A final wash was performed with methanol and then the black powder was dried with diethyl ether to afford 63 mg of oxidized GCB. GCB was also oxidized at 1% w/w as previously described [35].

1.3 Nanocomposite preparation

After the oxidation step, each carbon nanomaterial was used to prepare nanocomposites as previously described for GCB [35]. Briefly, 150 mg of each material were reacted with $\text{FeCl}_3 \cdot 6\text{H}_2\text{O}$ (810 mg), trisodium citrate (150 mg), sodium acetate (3.6 g), and poly(ethylene glycol)-10k (1.0 g) in 40 ml of ethylene glycol solution. Sonication was performed for 3 hours, then the mixture was sealed in a 125 mL autoclave at 200 °C for 10 hours. Next, after cooling to room temperature, the product was washed first with deionized water and then with ethanol. Next, sonication was performed for 30 minutes on 30 mg of the product in 50 mL of isopropyl alcohol, and 20 μL of diethylamine were added to the mixture and stirring was performed for 5 min. Next, 1.5 mL of titanium isopropoxide were added to the mixture, which was transferred to the autoclave for another 24 hours at 200 °C. The final materials were washed first with deionized water and then with ethanol and dried. Finally, the nanocomposites were calcined for 2 hours at 400 °C.

1.4 Molecular modelling

All models were computed with the GFN-xTB method (Geometry, Frequency, Non-covalent, eXtended Tight-Binding), a semiempirical method developed by Grimme et al. that allows computing efficiently systems with thousands of atoms [39]. This model has been reparameterized and enhanced with the recent, state of the art, intermolecular interactions [40]. Geometries were initially optimized with the GFN1 model which has a longer interaction range and refined with the GFN2 model that has improved electrostatics and dispersion.

1.5 Cancer cell lysate preparation

HeLa cells (100×10^6 cells) were resuspended in 10 mL of lysis buffer (8 mol L^{-1} urea in 50 mmol L^{-1} tris-HCl, pH 8, added with 1 tablet cOmplete™, Mini, EDTA-free Protease Inhibitor Cocktail (Sigma-Aldrich) and 1 tablet PhosSTOP (Sigma-Aldrich). Cells were vortexed and kept on ice for 15 min. To complete the lysis process, the sample was sonicated and kept on ice 10 times, then it was centrifuged at $20,000 \times g$ at 4 °C for 15 min to sediment cell debris. The supernatant was withdrawn and quantified by the Bradford assay. Nine hundred μg aliquots were then prepared and digested as previously described [35].

1.6 Phosphopeptide enrichment protocol

Lyophilized samples were reconstituted in 150 μL of the loading buffer (28% lactic acid, 57% MeCN, 14% H_2O , 0.2% TFA). The general enrichment procedure was as follows: after weighting an appropriate amount of suitable magnetic carbon material, the phase was conditioned with 100 μL of washing buffer (MeCN/ H_2O , 80:20 with 0.4% TFA) under gentle agitation for 2 min. After this and following steps, a 2 min centrifugation ($2300 \times g$) was performed to settle drops adhering to the vial and then the magnet was applied to retrieve the magnetic phase. Time and speed were increased to 5 min and $20,000 \times g$ in the case of CNT and CNH composites, to compact the phase and avoid losses. The supernatant was removed and a second conditioning with the loading buffer was performed. After this step, the peptide sample was added and gently shaken for 30 min. Then, the supernatant was discarded and the phase washed once with the loading buffer and twice with the washing buffer (100 μL each, 2 min shaking). Bound peptides were eluted twice with 100 μL of elution buffer 1 (1.5% NH_3 (aq)) and twice with 100 μL of elution buffer 2 (5% pyrrolidine (aq)), each time gently shaking for 5 min. Combined eluates were acidified with 2.5% TFA to pH 2.5, desalted, dried down in a Speed-Vac SC250 Express (Thermo Savant, Holbrook, NY, USA) and dissolved with 100 μL 0.1% formic acid. Samples were stored at -80 °C until analysis. For each experiment type, two experimental replicates were performed. For comparison purposes, enrichment was performed on commercial Pierce™ TiO_2 Phosphopeptide Enrichment and Clean-up Kit (ThermoFisher Scientific) according to manufacturer's instructions.

1.7 NanoHPLC-MS/MS analysis

For each sample, 20 μL were analyzed as described previously [35], with modifications on the MS method as described [36]. Briefly, full scan and MS/MS analysis of eluting peptides were performed by a Orbitrap Elite

hybrid ion trap-Orbitrap mass spectrometer (Thermo Scientific, Bremen, Germany) in the m/z range of 380-1400 Da and 30,000 (Full Width Half Maximum at m/z 400) resolution for the full scan and 15,000 resolution for MS/MS in top 10 data dependent mode. For each sample, three technical replicates were performed and the experiments were run twice.

1.8 Peptide identification

The acquired raw MS/MS data files from Xcalibur software (version 2.2 SP1.48, Thermo Fisher Scientific) were searched against Uniprot database by Proteome Discoverer software (version 1.3, Thermo Scientific) and the Mascot (v.2.3.2, Matrix Science) search engine, as previously described, using the human taxonomy (20284 entries).

2. Results and Discussion

2.1 Nanocomposite preparation

Nanocomposite preparation consisted of three steps: carbon nanostructure oxidation, magnetization, and growth of anatase titania NPs. Each step was monitored by TGA, Raman and FT-IR spectroscopy, and TEM imaging.

2.1.1 Carbon nanostructure oxidation

Carbon nanomaterials are notoriously hydrophobic, thus their oxidation reduced their propensity to aggregate to achieve dispersibility in water. To this end, oxidation procedures were optimized for each structure (*i.e.*, CNT, G, CNH, GCB), since their reactivity is strongly influenced by morphological parameters, such as number of graphitic layers, curvature, and so on. In this manner, each carbon material was oxidized to the same level, as assessed by thermogravimetric analysis (TGA) under nitrogen gas, corresponding to a weight loss of ca. 10 wt.% at 600 °C, and 2.3 ± 0.2 mmol COOH/g (see Fig. S1, ESM). In addition, oxidation served also to purify the materials, which were characterized by Raman spectroscopy (Figs. S2, ESM) and TEM micrographs, confirming preservation of their structure and loss of the amorphous carbon that was clearly visible on the surface of pristine CNTs and G (see Fig. 1).

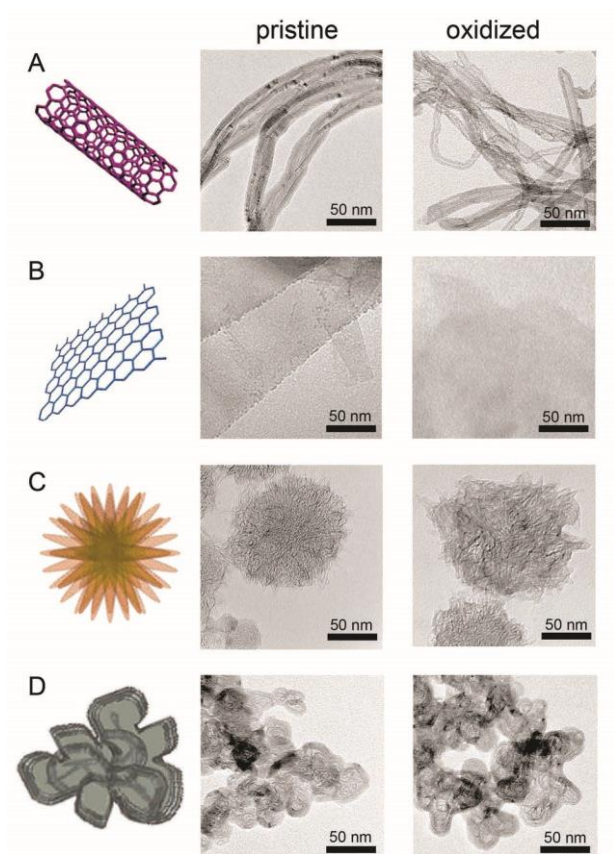


Figure 1 Transmission electron microscopy (TEM) micrographs of each carbon nanostructure in the pristine and oxidized state. A) carbon nanotubes (CNTs); B) graphene (G) and its oxide (GO); C) carbon nanohorns (CNHs); D) graphitized carbon black (GCB).

2.1.2 Magnetization of each scaffold

The second step was the magnetization of the nanomaterials. TEM imaging revealed iron oxide NPs homogeneous in size and spherical morphology, regardless of the carbon nanostructure used (Fig. 2A-D, Fig. S3 and Table S1, ESM). Importantly, magnetite NPs were observed only associated with the carbon nanostructures, thus confirming successful anchorage onto the scaffold, as dictated by design. The characteristic magnetite FT-IR signal at 600 cm^{-1} and Raman-active band at 670 cm^{-1} were

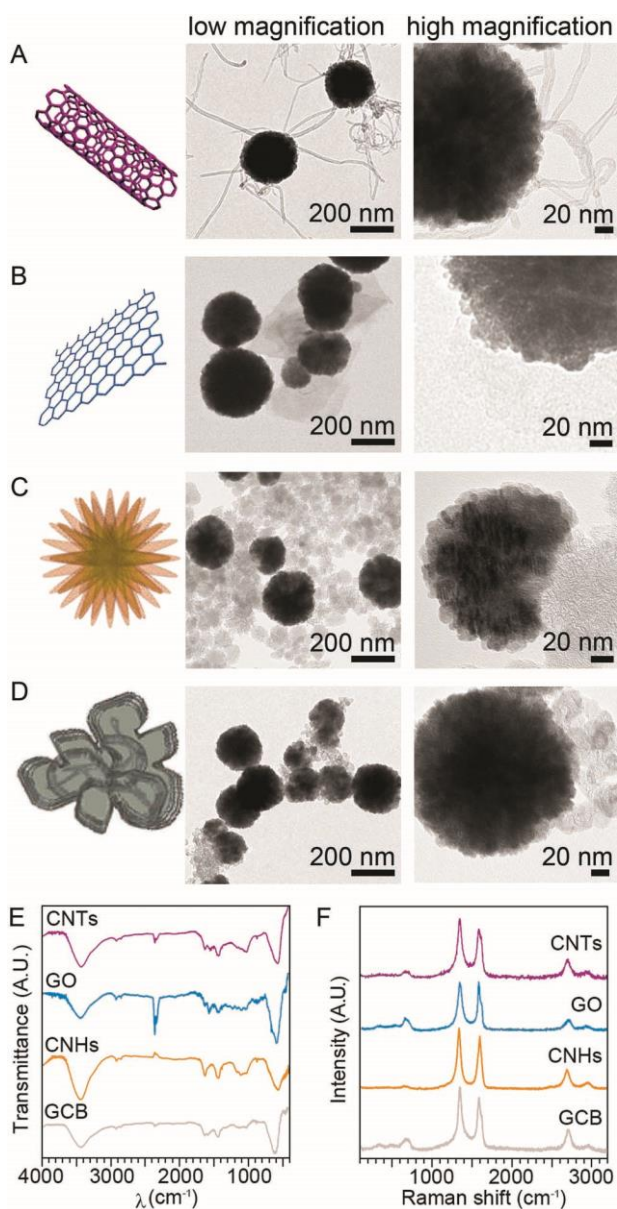


Figure 2 Magnetization of the carbon nanostructure scaffolds. TEM micrographs reveal magnetite spherical NPs on CNTs (A), GO (B), CNHs (C), and GCB (D). E) FT-IR spectra and (F) Raman spectra of each magnetized carbon nanostructure sample.

visible (Fig. 2E-F). A vibrating-sample magnetometer (VSM) determined magnetic properties (Fig.S4, Table S2, ESM), and efficient magnetic separation was visible by eye (Fig. S5, ESM). All samples were superparamagnetic since neither residual magnetization nor coercivity were detected. Iron oxide particles with the average diameters between 180 and 210 nm (Table S1, ESM) were composed of a large number of nanocrystallites under 20 nm in diameter as revealed by high-resolution TEM images (Fig. S6, ESM). Relatively high saturation magnetizations of all magnetic samples confirmed the capability to magnetically guide and separate magnetic nanocomposites by exposure to an external permanent magnet (Fig. S5). TGA under air confirmed increase of inorganic residue at 800 °C (Fig. S7 and Table S3, ESM).

2.1.3 Titania NP nucleation and growth

The last step consisted of titania NP growth onto the magnetized carbon nanomaterials. The nanocomposites were characterized by TEM, FT-IR, Raman, XRD spectroscopy (Fig. 3 and Fig. S8, ESM), and Zeta potential (Table

S4, ESM). Anatase presence was confirmed by XRD, FT-IR and Raman spectroscopies, with the characteristic FT-IR broad signal at 500-600 cm^{-1} and Raman bands at 147, 198, 396, 516, and 639 cm^{-1} . Inorganic residue increased up to 95-97 wt.% by TGA in air for the composites CNTs, CNHs, or GCB scaffolds, and to a minor 82 wt.% in the case of GO (see Table S3). Titania NP morphology (Fig. 3A-D) was different across samples and was remarkably affected by the scaffold structure, in contrast with what described above for magnetite NPs. In the case of CNHs, titania NPs completely covered the CNH clusters surface and TEM imaging revealed a characteristic morphology [35] with sharp elongated structures reminiscent of the morphology of the CNH scaffold underneath. In all the other cases, titania formed in geometric NPs with a rather large size distribution for GCB and CNTs. By contrast, in the case of GO, the scaffold was completely covered by very small and homogenous NPs with a narrow size distribution, corresponding to NP shorter axis of 9.0 ± 1.9 nm and longer axis of 17.3 ± 3.2 nm ($n = 100$). These results suggest GO played a special role in favoring anatase nucleation to produce NPs with enhanced surface area, as already observed for zeolite nanocrystals

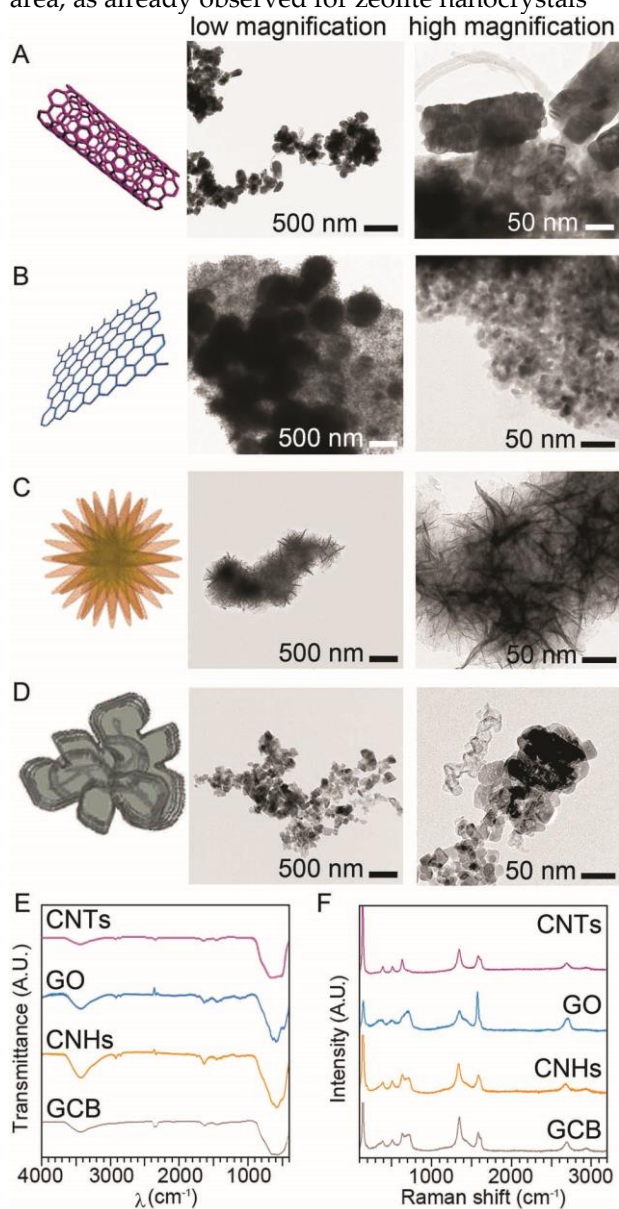


Figure 3 Final nanocomposites with titania NPs. TEM micrographs reveal different NP size on CNTs (A), GO (B), CNHs (C), and GCB (D). E) FT-IR spectra and (F) Raman spectra of each composite sample.

grown onto G [41]. Use of carbon nanostructures as scaffolds to achieve size- and shape-control over inorganic nanocrystal growth into hybrid materials is particularly attractive for applications in photocatalysis, and thus worth further investigations. To shed further light onto this interesting observation, *in silico* studies were performed as described below.

2.2 *In silico* studies of titania growth onto GO

Recent experimental and *in silico* investigations have focussed on the interfaces of single-crystal titania, rutile and anatase phases, with G and GO [42]. These studies revealed that the binding of flat monocrystalline TiO_2 was four times stronger for G than for GO. In addition, charge transfer, which could enhance the interaction, was computed and found to be very low in all cases. In contrast, the observed experimental morphology of TiO_2 on GO described above could be considered indication that moieties in GO could act as nucleation sites for the formation of titania nanocrystals. To study this effect, the interaction was modelled of a $(\text{TiO}_2)_2$ system [43], representing an early stage of the nucleation process, with different oxidized moieties on a GO flake.

A graphene hexagonal flake with a closed-shell ground state containing 222 carbon atoms and 2.8 nm diameter was chosen as substrate. The use of flakes, as opposed to periodic systems, allows studying explicitly adsorption edge effects and different side adsorption, as well as local deformations of curvature. Three different kinds of oxidized groups were considered, namely: epoxide, carboxyl, and alcohol functional groups together with a 2- Csp^3 defect as a very simplified model of generic chemical functionalization, Fig. 4. The number and positions of these groups was chosen so

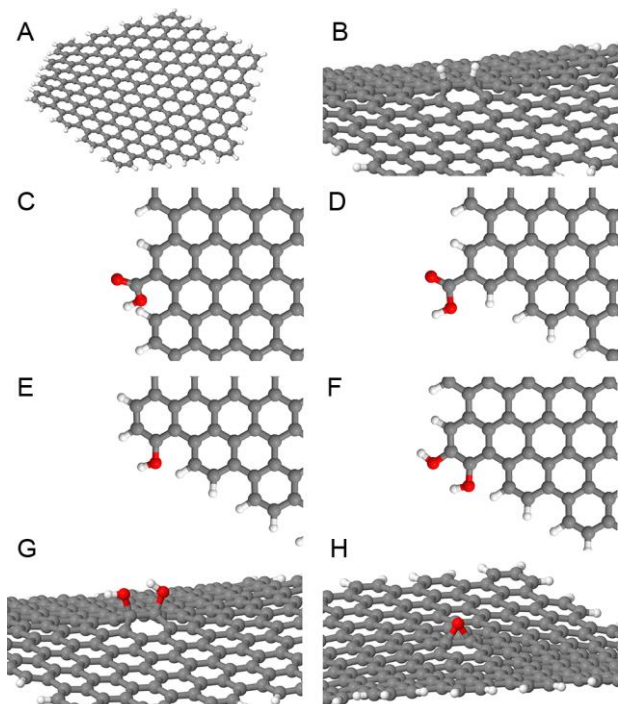


Figure 4 G (A,B) and GO (C-H) flakes used in the simulations with oxygen (red) functionalization models.

that the resulting system had no radicaloid character, *i.e.*, it is chemically stable. Three different initial positions for the $(\text{TiO}_2)_2$ adsorbates were considered: edge adsorption (near edge functional groups), on top of the flake (co-facial with the central area functional groups) and on the opposite, bottom-side of the flake (anti-facial). These positions were minimized and binding energies were computed. The results were consistent in terms of both binding energies and geometries found: the binding far from functional groups, which represents TiO_2 -G interactions, was in all cases around 3.5 eV (1.5 eV per TiO_2 molecule). When interacting with functional groups, the strongest binding was found at the edges, where most functional groups yielded bindings of 6.4 eV, which

was almost double the value for pristine G. This enhanced stabilization was due to the transfer of a hydrogen atom to one of the more basic, under-coordinated oxygen atoms from $(\text{TiO}_2)_2$.

Interestingly, carboxylic functional groups in two different positions of the GO flake, Fig. 4C-D, yielded binding energies differing by 0.9 eV, as shown in Fig. S9 of the ESM. This finding was due to the fact that, in one case, the $-\text{COOH}$ group could not adopt a linear conformation due to steric hindrance adding a penalty energy to the binding.

When considering co-facial adsorption geometries, the three internal functionalizations (Fig. 5)

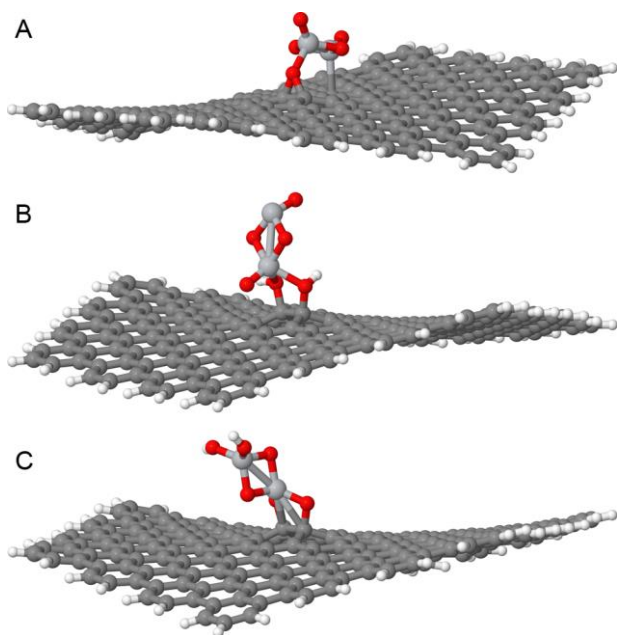


Figure 5 Co-facial binding of $(\text{TiO}_2)_2$ with either an epoxide (A), or two neighbouring alcohol groups, protonated (B) or not (C).

presented the highest binding energies. The strongest binding group was the epoxide group with 4.1 eV (Fig. 5A). The other two groups had very similar binding energies: 3.7 eV (2 $-\text{H}$) and 3.8 eV (2 $-\text{OH}$). Interestingly, optimization with tighter optimization thresholds, induced the migration of both alcohol H atoms to under-coordinated oxygen atoms of $(\text{TiO}_2)_2$ increasing the binding energy to the highest value found in this study, 8.3 eV, Fig. 5C.

Interestingly, the three internal functionalization models (Fig. 4B, 4G, and 4H) had also some of the highest binding energies when $(\text{TiO}_2)_2$ adsorption was anti-facial, that is, on the opposite side of G from the functional groups. The lowest binding corresponded to the epoxide group with 3.7 eV. The other two groups had more similar binding energies:

4.0 eV (2 $-\text{H}$) and 4.15 eV (2 $-\text{OH}$). Remarkably, this finding clearly shows that the binding on both sides of graphene, co-facial to functionalization, and anti-facial to functionalization, have comparable binding strengths. Summing up, in the strongest binding modes, one or two hydrogens atoms from the alcohol or carboxyl moieties migrated to be bonded to under-coordinated oxygen atoms of $(\text{TiO}_2)_2$. GO edge functional groups were systematically found to be strong binding sites for TiO_2 . These findings might help rationalize the fact that GO, being a 2D material, showed extensive coverage by titania. Importantly, it was found that in many cases, the oxygen atoms from the functional group directly coordinated with Ti atoms. This, by adding these atoms into the oxygen sub-lattice of TiO_2 NPs, may make them work as chemical anchorages for tethering the NPs in fixed positions. These binding modes might be related to the preferred nucleation, over growth, of numerous and small titania NPs over the surface of GO, in contrast with all the other carbon nanomaterials tested. In addition, the unexpected fact that opposite-side functional groups also showed improve binding with TiO_2 could also contribute to a fundamental feature of GO which may present double-side functionalization while other

nanocarbons can only be functionalized on their external surfaces.

2.3 Phosphoproteomics studies

Each nanocomposite material was tested for enrichment of phosphopeptides extracted from cancer cells, whose lysates provide a realistic and highly complex biological sample model [44]. Given that the ratio between loaded sample and (nano)material amount strongly affects the performance of the system, two amounts were tested (*i.e.*, 3 mg and 5 mg). The enrichment was performed by directly loading the protein digest onto the nanocomposites to keep the number of manual operations, hence experimental error, to a minimum. The results were compared against a TiO₂-based commercial product (*i.e.*, spin column) and are reported in Fig. 6, S10, S11 (ESM). Important parameters to assess the nanocomposite performance include: 1) selectivity of phosphopeptide binding (Fig. 6A); 2) total number of (phospho)peptides detected (Fig. 6B); 3) efficiency of analyte binding (*i.e.*, log₂ average intensity of MS signal, Fig. S10 of ESM); 4) type of phosphopeptide enriched by each nanocomposite (Fig. 6C-D and Fig. S11, ESM).

Selectivity was calculated based on the percent ratio of phosphorylated peptides relative to the total number of detected peptides. The commercial product displayed a selectivity of 60%, which was enhanced to nearly 90% in the case of the GO nanocomposite, followed by the CNH nanocomposite (71%), as shown in Fig. 6A. This result can be rationalized based on the fact that these two materials displayed the smallest titania nanocrystals with a narrow size distribution (see Fig. 3B-C), which corresponded to a relatively higher surface area for phosphopeptide contact, as confirmed by BET analysis (see Table 1). However, high selectivity came at the expense of total peptide identifications. In this regard, CNT and GCB scaffolds led to a performance overall similar to the commercial product at their best condition.

Interestingly, reducing the oxidation level of GCB down to 1 wt.% significantly enhanced the number of total peptide identifications, reaching consistently over 6,000 hits (Fig. 6B). Total peptide binding is an important factor, especially for the proteomic profiling of biological samples towards advanced disease diagnostics.

In terms of efficiency of analyte binding (*i.e.*, log₂ average intensity of MS signal, Fig. S10, ESM), the performance of all nanocomposites was overall similar. Notably, also in this case the commercial

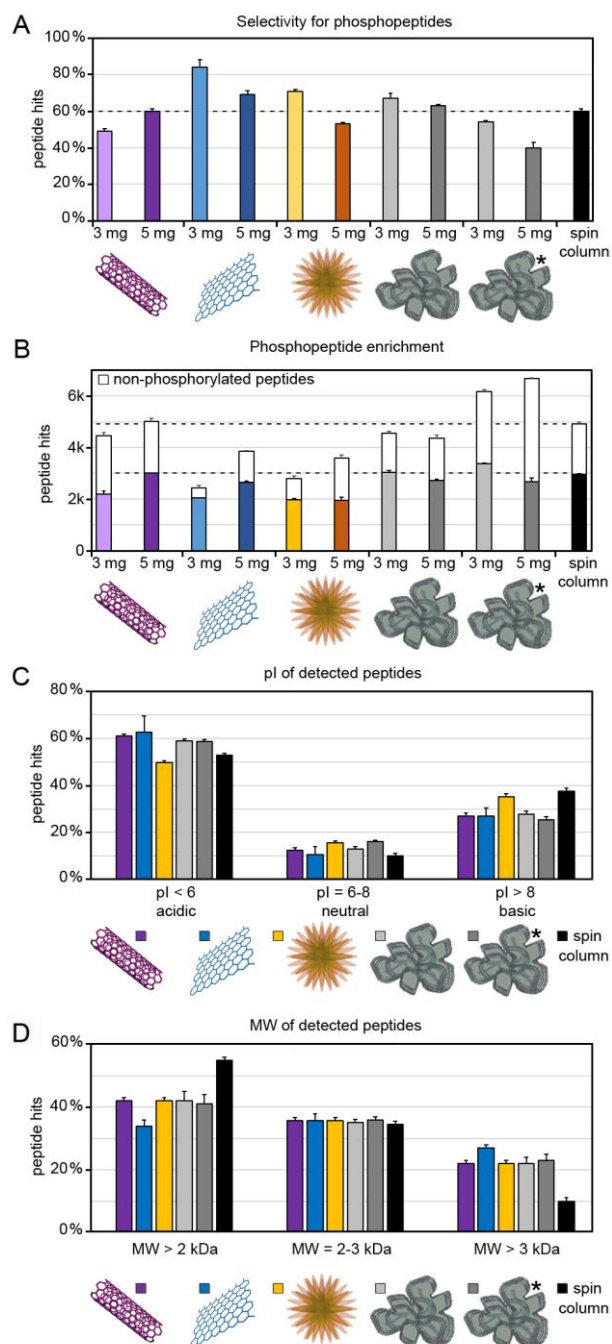


Figure 6 Phosphoproteomics study. A) phosphopeptide selectivity; B) number of peptide and phosphopeptides detected; C) isoelectric point (pI) of peptide hits; D) molecular weight (MW) of peptide hits. * denotes GCB oxidized at 1 wt. %.

product performance was surpassed by the GO nanocomposite (that also displayed the highest selectivity) and the nanocomposite based on GCB with a low-oxidation level (that also displayed the highest number of peptide identifications). The maximum at log₂(average intensity) corresponded to 23 (GO) and 22 (GCB), *versus* 20 for the reference (Fig. S10 of ESM).

To assess if any difference was present in terms of type of peptides isolated by the different materials, three parameters were evaluated: the grand average of hydropathy (GRAVY) index (Figure S11, ESM), the isoelectric point (pI, Fig. 6C), and the molecular weight (MW, Fig. 6D). Most of the identified peptides, regardless of the phosphorylation state, were hydrophilic for any composite, with GRAVY values ≤ 0 for well over 90% of the

recovered peptides (Fig. S11 of ESM). pI analysis revealed that most of the identified peptides were acidic ($pI < 6$), and only minor differences between nanocomposites were noted (Fig. 6C). Some difference could be appreciated in MW distribution (Fig. 6D). Smaller peptides with a MW in the range of 1-3 kDa composed the majority of analyte hits. However, the use of any nanocarbon as scaffold led to the over double the number of recovered peptides with MW > 4 kDa relative to the commercial reference. This is a positive effect considering that most phosphopeptides could be larger than common tryptic peptides, due to the higher possibility of missed cleavages [45].

Porosimetry analysis was thus performed to gain further insights in the different performance of the nanocomposites (Table 1). All of them were mesoporous, although to a different extent. The best results in terms of total phosphopeptide identifications were obtained with the least oxidized

Sample	Surface area ($\text{m}^2 \text{g}^{-1}$)	Pore volume ($\text{cm}^3 \text{g}^{-1}$)	Porosity	Pore size (\AA)
CNT	29.5 ± 0.5	0.102	little mesoporous	20-500
GO	45.1 ± 0.5	0.139	mesoporous	20-300
CNH	37.6 ± 0.5	0.178	mesoporous	10-500
GCB	53.2 ± 0.5	0.210	little mesoporous	20-500
GCB*	22.6 ± 0.5	0.085	very little mesoporous	20-40

Table 1 Porosimetry analysis of the nanocomposite materials. *GCB oxidized at 1 wt. %.

GCB composite, which also had the smallest pore volume and size. We inferred that the lack of extensive porosity of the surface positively affected the interaction between the TiO_2 layer and the phosphopeptides, suggesting that the process of phosphopeptide enrichment did not involve migration into and out of the pores and was thus favored for the least porous materials.

3. Conclusions

This study assessed the effects of the different nanomorphology of CNT, GO, CNH, and GCB on their templating activity for the preparation of magnetized TiO_2 nanocomposites for phosphoproteomics. During the first magnetization step, no significant difference was noted on the growth of magnetite NPs in terms of their size and morphology. By contrast, growth of titania at the subsequent step was significantly affected by each scaffold, resulting in heterogeneously shaped and sized anatase NPs. Importantly, only in the case of GO as scaffold, highly homogenous and few-nm wide NPs were obtained, which covered completely the graphitic surface. *In silico* investigations supported a role of the oxygen atoms of GO in favoring nucleation of TiO_2 NPs through direct coordination with the Ti atom. In other words, the oxygen-containing functional groups of GO acted as chemical anchorages for tethering the NPs in fixed positions, thus favoring NP nucleation over growth. Being GO the only carbon nanostructure tested that may have double-side functionalization, and having opposite-side functional groups also binding TiO_2 , a fundamental difference arose between GO and the other scaffolds on the NP growth. This finding could be interesting for a number of titania applications also beyond the scope of this study, such as in the area of water remediation and catalysis.

Finally, the performance of the nanocomposites was assessed in shotgun phosphoproteomics in a complex matrix. The reference commercial product was surpassed by all parameters evaluated, *i.e.*, selectivity, total hits, and intensity of MS signal. The highest selectivity was reached by the GO-based nanocomposites (nearly 90%),

followed by the CNH-based materials (71%), although at the expense of total hits. On the other hand, maximization of phosphopeptide identifications was achieved with the GCB nanocomposite with low oxidation level. Such behavior could be ascribed to the nanostructure mesoporosity. Generally, the nanocarbon-based composites with the lowest porosity were the ones providing the largest number of phosphopeptide identifications, suggesting that analyte binding did not require migration into and out of the pores. An additional advantage of the nanocarbon-based composites over the commercial product was the ability to recover larger peptides, with MW > 3 kDa.

Overall this study provided the first thorough assessment of different carbon nanomaterial scaffolds for functional composites in phosphoproteomics studies including their performance in realistic biological samples with a high level of complexity. This data advanced the understanding not only of the nucleation and growth of NPs onto the scaffolds towards high-quality functional composites, but it also revealed details of surface properties that are beneficial for the design of innovative nanocomposites with improved performance.

Acknowledgements

This work was supported by PRIN 2015, project number 2015TWP83Z. The authors would like to acknowledge networking support by the COST Action MultiComp CA15107, as well as financial support from the Slovenian Research Agency (ARRS) for research core funding No. (P2-0089) and projects No. (J1-7302 and J3-7494).

Electronic Supplementary Material: Supplementary material (additional TEM images, XRD, VSM, TGA and Raman data, NP diameter measured by TEM, *in silico* and proteomics data and photographs of magnetic separation) is available in the online version of this article at http://dx.doi.org/10.1007/10.1007/s12274-***-****-* and is accessible free of charge

References

- [1] Malik, S.; Krashennikov, A. V.; Marchesan, S. Advances in nanocarbon composite materials, *Beilstein J. Nanotechnol.* **2018**, *9*, 20-21.
- [2] Eder, D. Carbon Nanotube–Inorganic Hybrids. *Chem. Rev.* **2010**, *110*, 1348-1385.
- [3] Pérez, E. M.; Martín, N. π - π interactions in carbon nanostructures. *Chem. Soc. Rev.* **2015**, *44*, 6425-6433.
- [4] Lonkar, S. P.; Deshmukh, Y. S.; Abdala, A. A. Recent advances in chemical modifications of graphene. *Nano Res.* **2015**, *8*, 1039-1074.
- [5] Karousis, N.; Suarez-Martinez, I.; Ewels, C. P.; Tagmatarchis, N. Structure, Properties, Functionalization, and Applications of Carbon Nanohorns. *Chem. Rev.* **2016**, *116*, 4850-4883.
- [6] Hirsch, A. Functionalization of single-walled carbon nanotubes. *Angew. Chem. Int. Ed.* **2002**, *41*, 1853-1859.
- [7] Kemnade, N.; Gebhardt, P.; Haselmann, G. M.; Cherevan, A.; Wilde, G.; Eder, D. How to Evaluate and Manipulate Charge Transfer and Photocatalytic Response at Hybrid Nanocarbon–Metal Oxide Interfaces. *Adv. Funct. Mater.* **2018**, *28*, 1704730.
- [8] Eder, D.; Windle, A. H. Carbon–Inorganic Hybrid Materials: The Carbon-Nanotube/TiO₂ Interface. *Adv. Mater.* **2008**, *20*, 1787-1793.
- [9] Melchionna, M.; Prato, M.; Fornasiero, P. Mix and match metal oxides and nanocarbons for new photocatalytic frontiers. *Catal. Today* **2016**, *277*, 202-213.
- [10] Saha, A.; Moya, A.; Kahnt, A.; Iglesias, D.; Marchesan, S.; Wannemacher, R.; Prato, M.; Vilatela, J. J.; Guldi, D. M. Interfacial charge transfer in functionalized multi-walled carbon nanotube@TiO₂ nanofibres. *Nanoscale* **2017**, *9*, 7911-7921.
- [11] Beltram, A.; Melchionna, M.; Montini, T.; Nasi, L.; Fornasiero, P.; Prato, M. Making H₂ from light and biomass-derived alcohols: the outstanding activity of newly designed hierarchical MWCNT/Pd@TiO₂ hybrid catalysts. *Green Chem.* **2017**, *19*, 2379-2389.
- [12] Wijeratne, A. B.; Wijesundera, D. N.; Paulose, M.; Ahiabu, I. B.; Chu, W.-K.; Varghese, O.K.; Greis, K.D. Phosphopeptide Separation Using Radially Aligned Titania Nanotubes on Titanium Wire. *ACS Appl. Mater. Interfaces* **2015**, *7*, 11155-11164.
- [13] Cutillas, P. R. Role of phosphoproteomics in the development of personalized cancer therapies. *Prot. Clin. Appl.* **2015**, *9*, 383-395.
- [14] Rainer, M.; Bonn, G. K. Enrichment of phosphorylated peptides and proteins by selective precipitation methods. *Bioanalysis* **2015**, *7*, 243-252.
- [15] von Stechow, L.; Francavilla, C.; Olsen, J. V. Recent findings and technological advances in phosphoproteomics for cells and tissues. *Expert Rev. Proteomic.* **2015**, *12*, 469-487.
- [16] Engholm-Keller, K.; Larsen, M. R. Technologies and challenges in large-scale phosphoproteomics. *Proteomics* **2013**, *13*, 910-931.
- [17] Beltran, L.; Cutillas, P. R. Advances in phosphopeptide enrichment techniques for phosphoproteomics. *Amino Acids* **2012**, *43*, 1009-1024.

- [18] Dunn, J. D.; Reid, G. E.; Bruening, M. L. Techniques for phosphopeptide enrichment prior to analysis by mass spectrometry. *Mass Spectrom. Rev.* **2010**, *29*, 29-54.
- [19] Wang, Z.-G.; Lv, N.; Bi, W.-Z.; Zhang, J.-L.; Ni, J.-Z. Development of the Affinity Materials for Phosphorylated Proteins/Peptides Enrichment in Phosphoproteomics Analysis. *ACS Appl. Mater. Interfaces* **2015**, *7*, 8377-8392.
- [20] Roberts, D. S.; Chen, B.; Tiambeng, T. N.; Wu Z.; Ge, Y.; Jin, S. Reproducible large-scale synthesis of surface silanized nanoparticles as an enabling nanoproteomics platform: Enrichment of the human heart phosphoproteome. *Nano Res.* **2019**, *12*, 1473-1481.
- [21] Deng, Z.; Zhao, Z.; Ning, B.; Basilio, J.; Mann, K.; Fu, J.; Gu, Y.; Ye, Y.; Wu, X.; Fan, J.; Chiao, P.; Hu, T. Nanotrap-enabled quantification of KRAS-induced peptide hydroxylation in blood for cancer early detection. *Nano Res.* **2019**, *12*, 1445-1452.
- [22] Sun, N.; Wu, H.; Shen, X.; Deng, C. Nanomaterials in Proteomics. *Adv. Funct. Mater.* **2019**, *29*, 1900253.
- [23] Araújo, J. E.; Lodeiro, C.; Capelo, J. L.; Rodríguez-González, B.; dos Santos, A. A.; Santos, H. M.; Fernández-Lodeiro, J. Novel nanocomposites based on a strawberry-like gold-coated magnetite (Fe@Au) for protein separation in multiple myeloma serum samples. *Nano Res.* **2015**, *8*, 1189-1198.
- [24] Fang, G.; Gao, W.; Deng, Q.; Qian, K.; Han, H.; Wang, S. Highly selective capture of phosphopeptides using a nano titanium dioxide-multiwalled carbon nanotube nanocomposite. *Anal. Biochem.* **2012**, *423*, 210-217.
- [25] Lu, J.; Deng, C.; Zhang, X.; Yang, P. Synthesis of Fe₃O₄/Graphene/TiO₂ Composites for the Highly Selective Enrichment of Phosphopeptides from Biological Samples. *ACS Appl. Mater. Interfaces* **2013**, *5*, 7330-7334.
- [26] Wang, M.; Deng, C.; Li, Y.; Zhang, X. Magnetic Binary Metal Oxides Affinity Probe for Highly Selective Enrichment of Phosphopeptides. *ACS Appl. Mater. Interfaces* **2014**, *6*, 11775-11782.
- [27] Scida, K.; Stege, P. W.; Haby, G.; Messina, G. A.; García, C. D. Recent applications of carbon-based nanomaterials in analytical chemistry: critical review. *Anal. Chim. Acta* **2011**, *691*, 6-17.
- [28] Melchionna, M.; Beltram, A.; Montini, T.; Monai, M.; Nasi, L.; Fornasiero, P.; Prato, M. Highly efficient hydrogen production through ethanol photoreforming by a carbon nanocone/Pd@TiO₂ hybrid catalyst. *Chem. Commun.* **2016**, *52*, 764-767.
- [29] Iglesias, D.; Melle-Franco, M.; Kurbasic, M.; Melchionna, M.; Abrami, M.; Grassi, M.; Prato, M.; Marchesan, S. Oxidized Nanocarbons-Tripeptide Supramolecular Hydrogels: Shape Matters! *ACS Nano* **2018**, *12*, 5530-5538.
- [30] Iijima, S.; Yudasaka, M.; Yamada, R.; Bandow, S.; Suenaga, K.; Kokai, F.; Takahashi, K. Nano-aggregates of single-walled graphitic carbon nano-horns. *Chem. Phys. Lett.* **1999**, *309*, 165-170.
- [31] Iglesias, D.; Giuliani, A.; Melchionna, M.; Marchesan, S.; Criado, A.; Nasi, L.; Bevilacqua, M.; Tavagnacco, C.; Vizza, F.; Prato, M.; Fornasiero, P. N-Doped Graphitized Carbon Nanohorns as a Forefront Electrocatalyst in Highly Selective O₂ Reduction to H₂O₂. *Chem* **2018**, *4*, 106-123.
- [32] Capriotti, A.L.; Cavaliere, C.; Foglia, P.; Samperi, R.; Stampachiaccchiere, S.; Ventura, S.; Laganà, A. Ultra-high-performance liquid chromatography-tandem mass spectrometry for the analysis of free and conjugated natural estrogens in cow milk without deconjugation. *Anal. Bioanal. Chem.* **2015**, *407*, 1705-1719.
- [33] Cavaliere, C.; Capriotti, A. L.; Ferraris, F.; Foglia, P.; Samperi, R.; Ventura, S.; Laganà, A. Multiresidue analysis of endocrine-disrupting compounds and perfluorinated sulfates and carboxylic acids in sediments by ultra-high-performance liquid chromatography-tandem mass spectrometry. *J. Chromatogr. A* **2016**, *1438*, 133-142.
- [34] Di Corcia, A.; Marchese, S.; Samperi, R. Evaluation of graphitized carbon black as a selective adsorbent for extracting acidic organic compounds from water. *J. Chromatogr. A* **1993**, *642*, 163-174.
- [35] Piovesana, S.; Capriotti, A. L.; Cavaliere, C.; Ferraris, F.; Iglesias, D.; Marchesan, S.; Laganà, A. New Magnetic Graphitized Carbon Black TiO₂ Composite for Phosphopeptide Selective Enrichment in Shotgun Phosphoproteomics. *Anal. Chem.* **2016**, *88*, 12043-12050.
- [36] La Barbera, G.; Capriotti, A. L.; Cavaliere, C.; Ferraris, F.; Montone, C. M.; Piovesana, S.; Zenezini Chiozzi, R.; Laganà, A. Saliva as a source of new phosphopeptide biomarkers: Development of a comprehensive analytical method based on shotgun peptidomics. *Talanta* **2018**, *183*, 245-249.
- [37] Li, X.-S.; Zhu, G.-T.; Luo, Y.-B.; Yuan, B.-F.; Feng, Y.-Q. Synthesis and applications of functionalized magnetic materials in sample preparation. *Trends Anal. Chem.* **2013**, *45*, 233-247.
- [38] Papi, M.; Palmieri, V.; Digiacomo, L.; Giulimondi, F.; Palchetti, S.; Ciasca, G.; Perini, G.; Caputo, D.; Cartillone, M. C.; Cascone, C.; Coppola, R.; Capriotti, A. L.; Laganà, A.; Pozzi, D.; Caracciolo, G. Converting the personalized biomolecular corona of graphene oxide nanoflakes into a high-throughput diagnostic test for early cancer detection. *Nanoscale* **2019**, *11*, 15339-15346.
- [39] Grimme, S.; Bannwarth, C.; Shushkov, P. A Robust and Accurate Tight-Binding Quantum Chemical Method for Structures, Vibrational Frequencies, and Noncovalent Interactions of Large Molecular Systems Parametrized for All spd-Block Elements (Z = 1-86). *J. Chem. Theory Comput.* **2017**, *13*, 1989-2009.
- [40] Christoph, B.; Sebastian, E.; Stefan, G. GFN2-xTB - an Accurate and Broadly Parametrized Self-Consistent Tight-Binding Quantum Chemical Method with Multipole Electrostatics and Density-Dependent Dispersion Contributions. *J. Chem. theory Comput.* **2019**, *15*, 1652-1671.
- [41] Gebhardt, P.; Pattinson, S. W.; Ren, Z.; Cooke, D. J.; Elliott, J. A.; Eder, D. Crystal engineering of zeolites with graphene. *Nanoscale* **2014**, *6*, 7319-7324.
- [42] Martins, P. M.; Ferreira, C. G.; Silva, A. R.; Magalhães, B.; Alves, M. M.; Pereira, L.; Marques, P. A. A. P.; Melle-Franco, M.; Lanceros-Méndez, S. TiO₂/graphene and TiO₂/graphene oxide nanocomposites for photocatalytic applications: A computer modeling and experimental study. *Compos. Part B-Eng.* **2018**, *145*, 39-46.
- [43] Hamad, S.; Catlow, C. R. A.; Woodley, S. M.; Lago, S.; Mejías, J. A. Structure and Stability of Small TiO₂ Nanoparticles. *J. Phys. Chem. B* **2005**, *109*, 15741-15748.
- [44] Sharma, K.; D'Souza, R. C. J.; Tyanova, S.; Schaab, C.; Wiśniewski, J. R.; Cox, J.; Mann, M. Ultradeep Human Phosphoproteome

Reveals a Distinct Regulatory Nature of Tyr and Ser/Thr-Based Signaling. *Cell Rep.* **2014**, *8*, 1583-1594.
[45] Solari, F. A.; Dell'Aica, M.; Sickmann, A.; Zahedi, R. P. *Mol. Biosyst.* **2015**, *11*, 1487-1493.

Electronic Supplementary Material

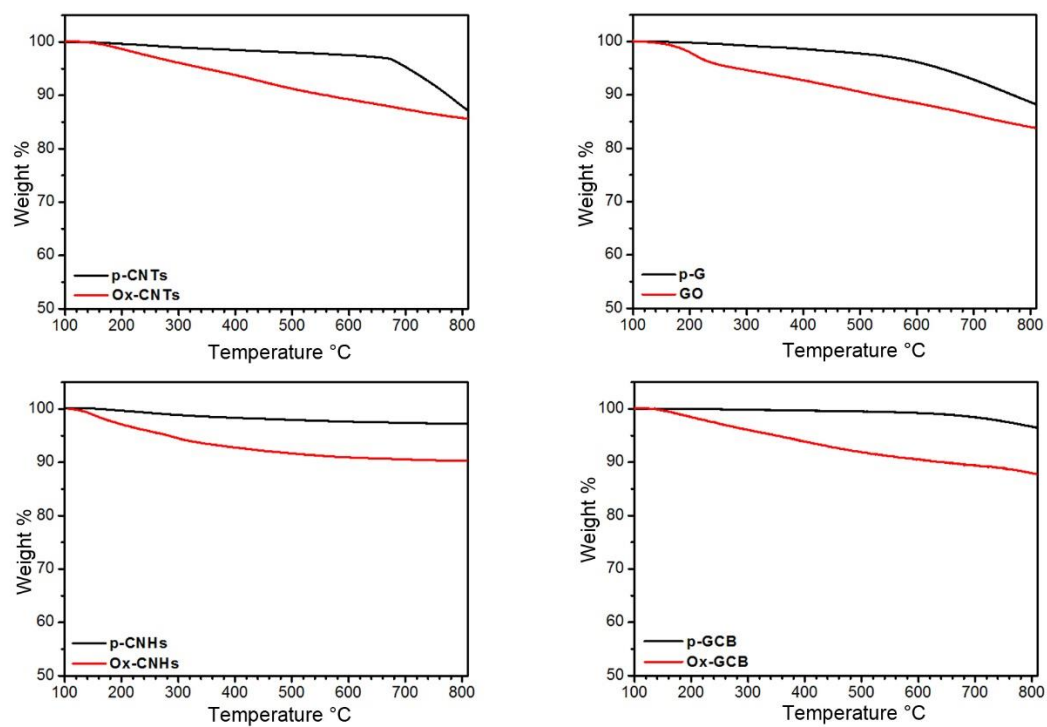


Fig. S1. Thermogravimetric analysis (TGA) of pristine and oxidized carbon nanostructures under nitrogen gas.

Anna L. Capriotti, annalaura.capriotti@uniroma1.it; Silvia Marchesan, smarchesan@units.it.

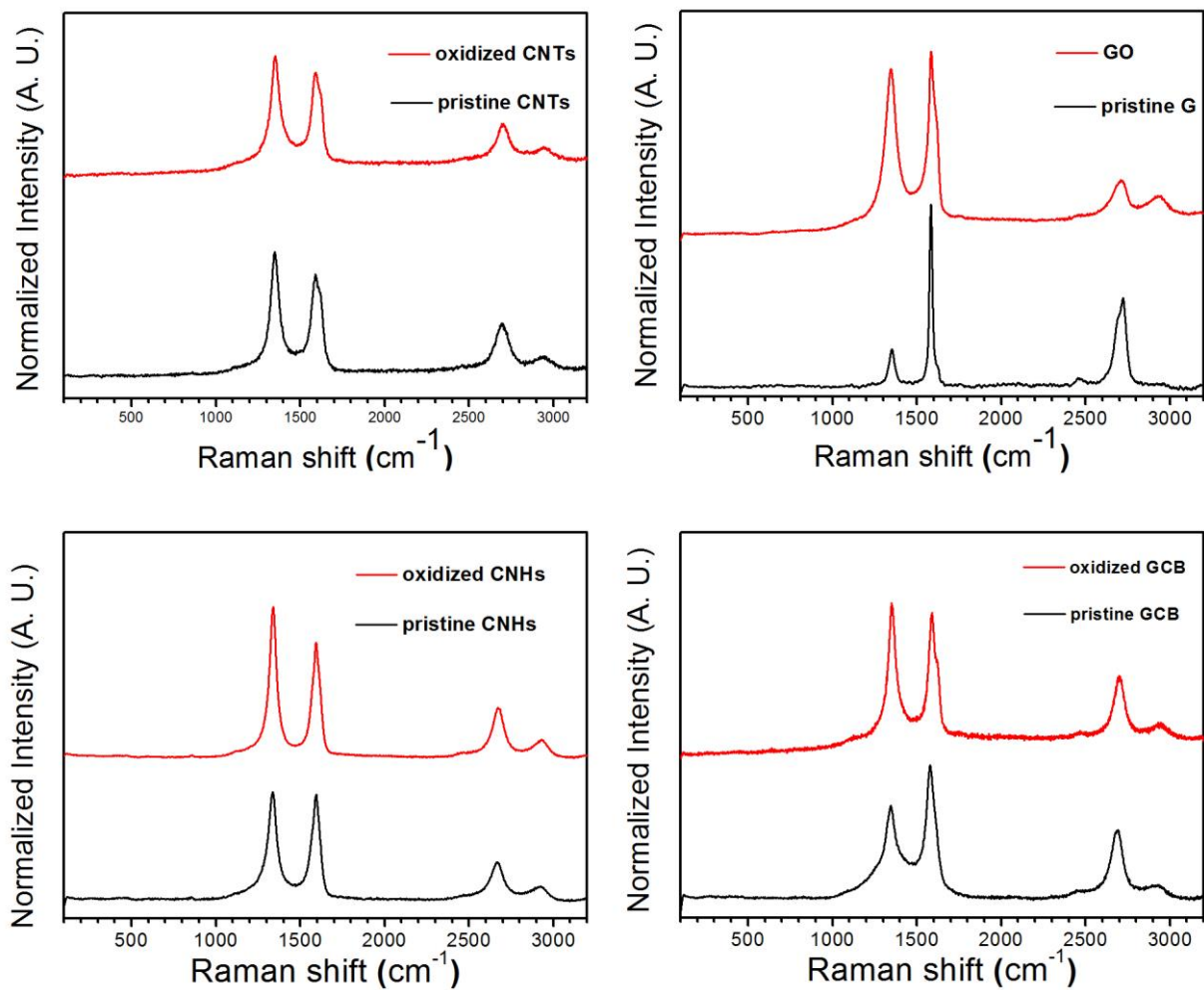


Fig. S2. Raman spectra of pristine and oxidized carbon nanostructures.

Oxidized CNTs	GO	Oxidized CNHs	Oxidized GCB
210 ± 43	192 ± 40	185 ± 37	180 ± 39

Table S1. Magnetite NP average diameter (nm) ± stdev (n = 100).

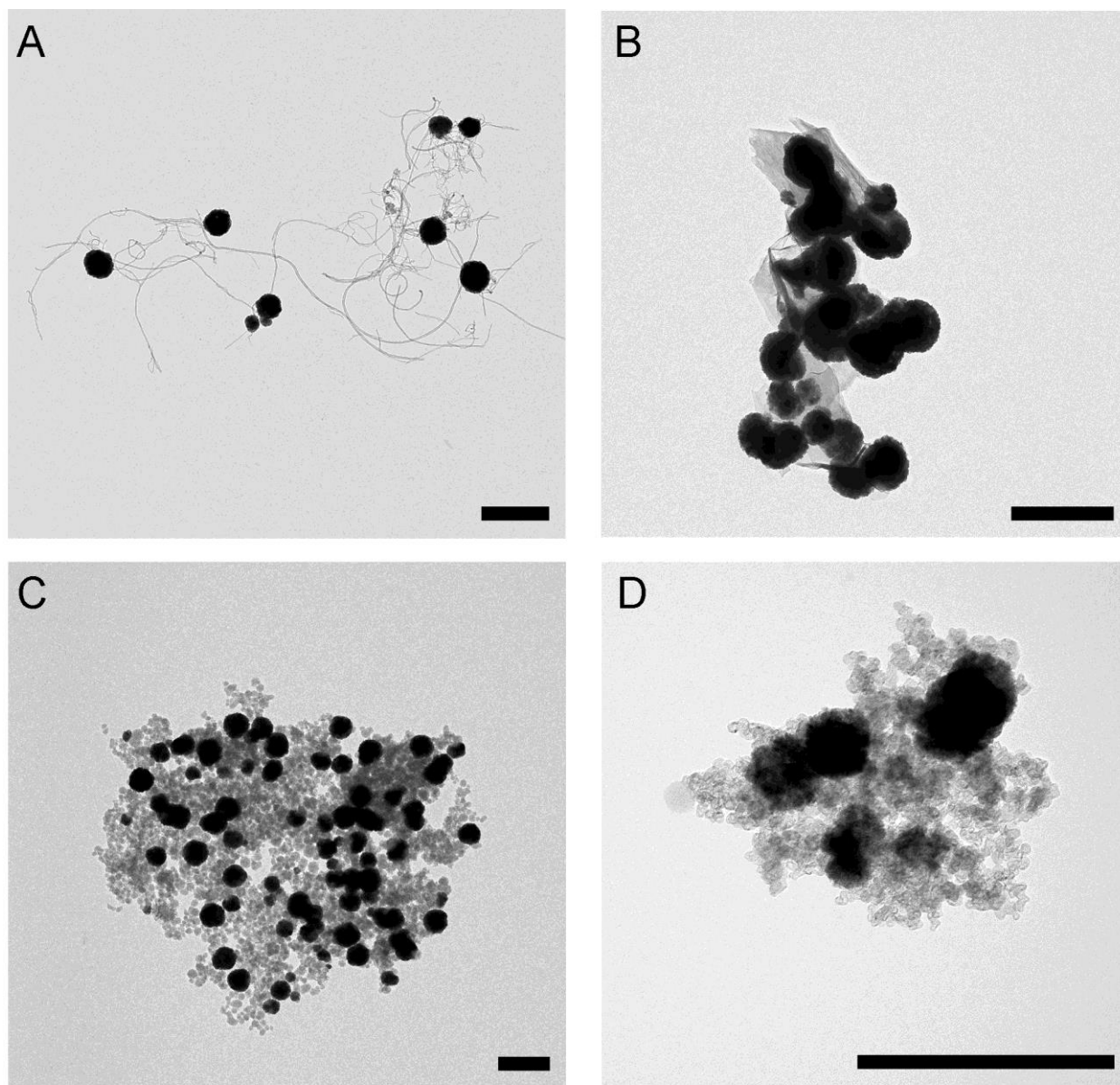


Fig. S3. TEM images of magnetite NPs anchored onto oxidized carbon nanostructures; A) CNTs, B) GO, C) CNHs, and D) GCB. Scale bar = 500 nm.

Sample	Saturation magnetization (Am^2/kg)
CNTs	44.5
GO	43.3
CNHs	40.2
GCB	52.2

Table S2. Saturation magnetization values obtained from VSM data for magnetized samples.

Sample	Pristine	Oxidized	Magnetized	Final titania composite
CNTs	1	1	59	97
G	4	0	63	82
CNHs	1	1	54	95
GCB	0	4	75	96

Table S3. TGA data (wt.% residue at 800 °C) under air for carbon nanomaterials.

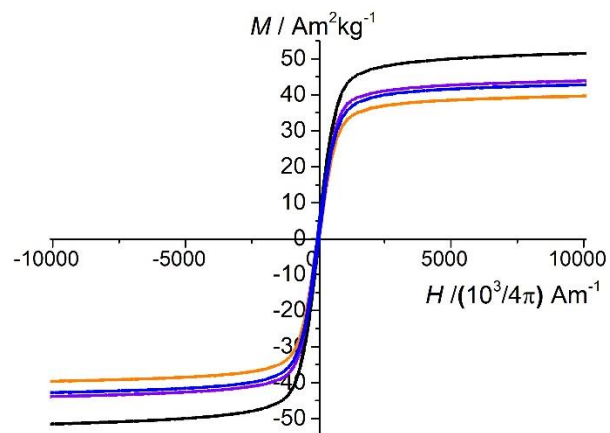


Figure S4. Room-temperature measurements of the mass magnetization as a function of magnetic field for the magnetized CNT (purple), GO (blue), CNHs (orange), and GCB (black).

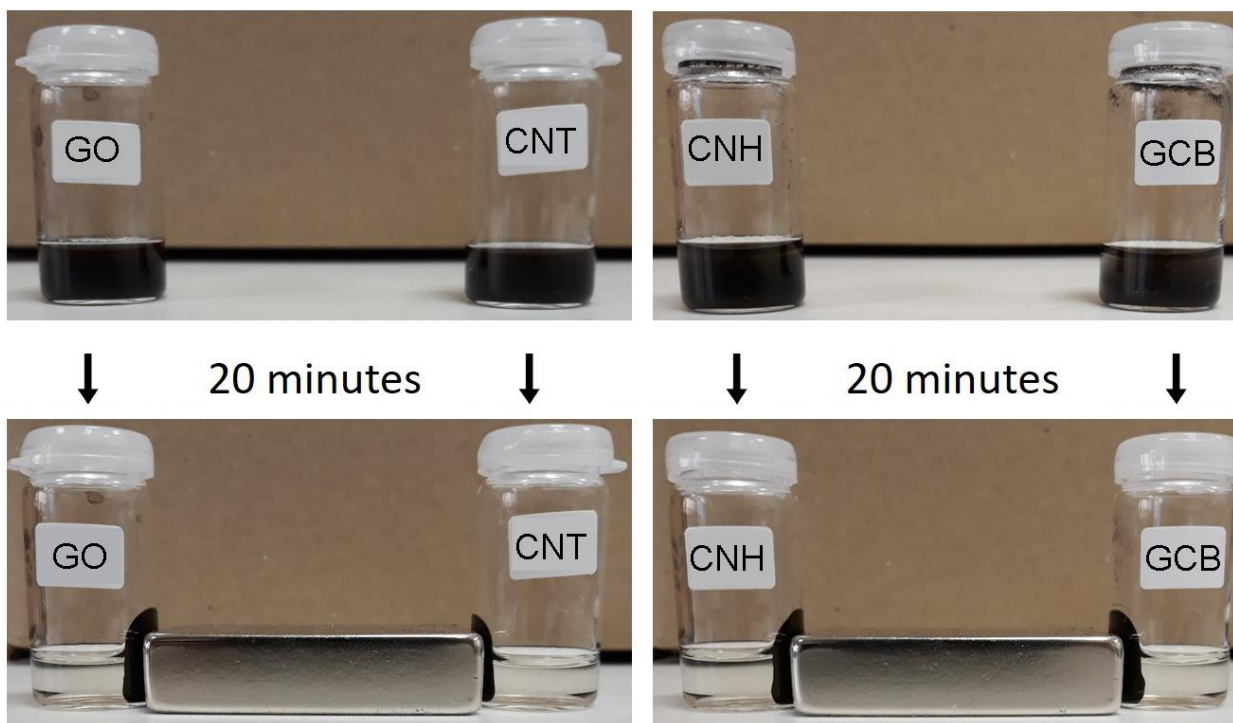


Fig. S5. Efficient magnetic separation is possible for all the magnetized samples after exposure to a permanent magnet.

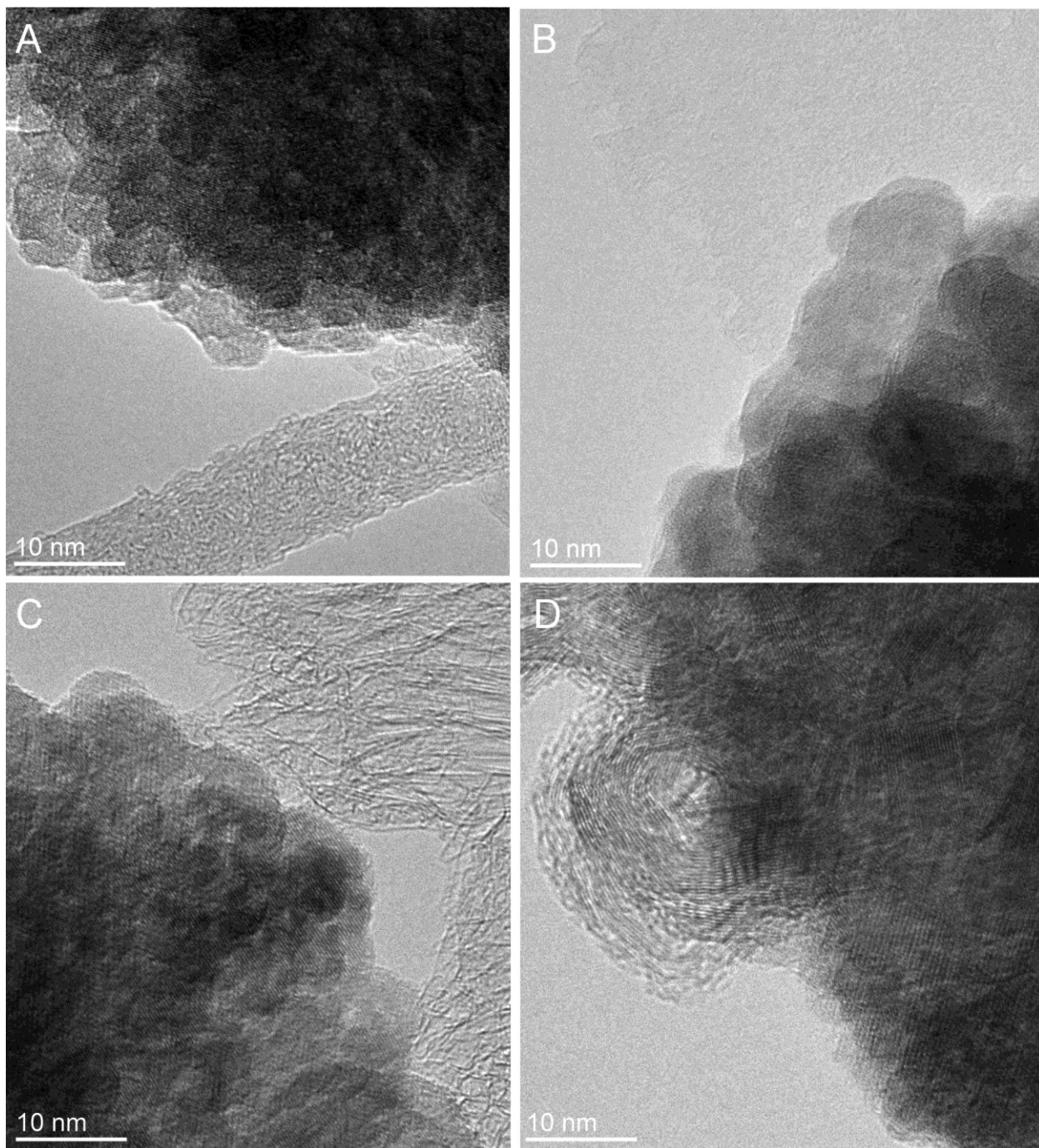


Fig. S6. High-resolution TEM images show nanocrystal clusters from magnetite NPs on A) CNTs, B) GO, C) CNHs, and D) GCB samples.

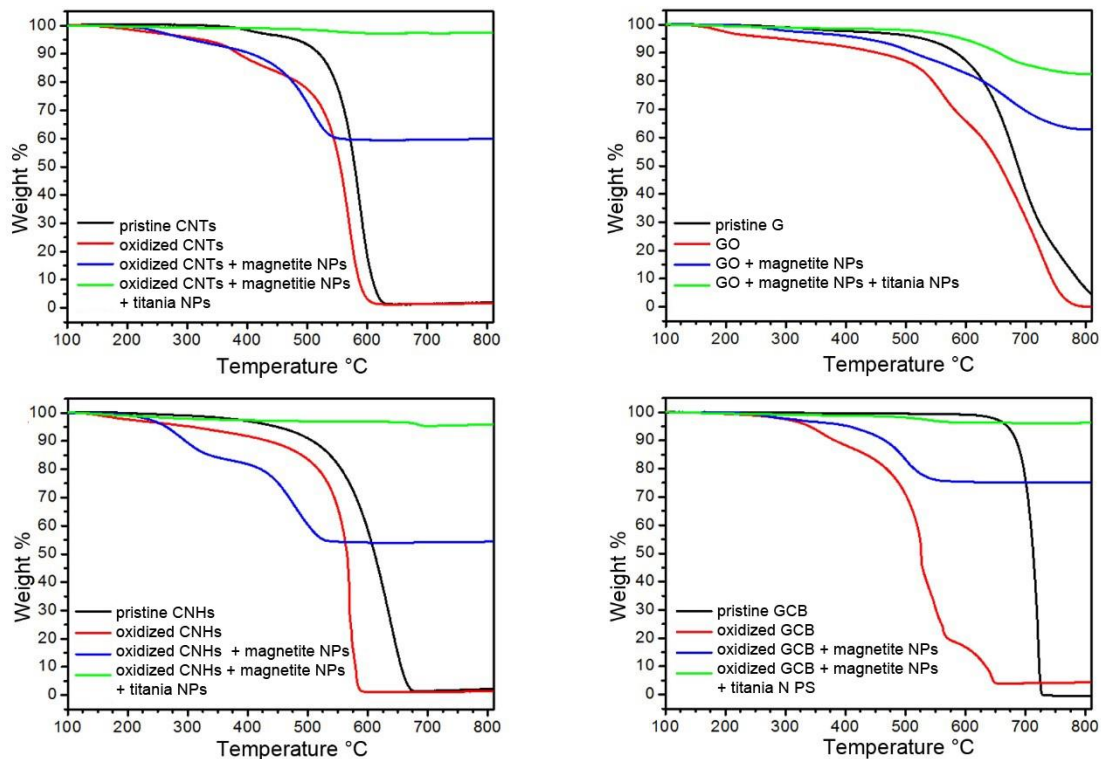


Fig. S7. TGA under air after each sample modification step.

Sample	Zeta potential (mV)
CNTs	-35.3 ± 2.35
G	-27.6 ± 7.30
CNHs	-25.2 ± 4.79
GCB	-28.5 ± 1.89

Table S4. Zeta potential data for the final nanocomposites.

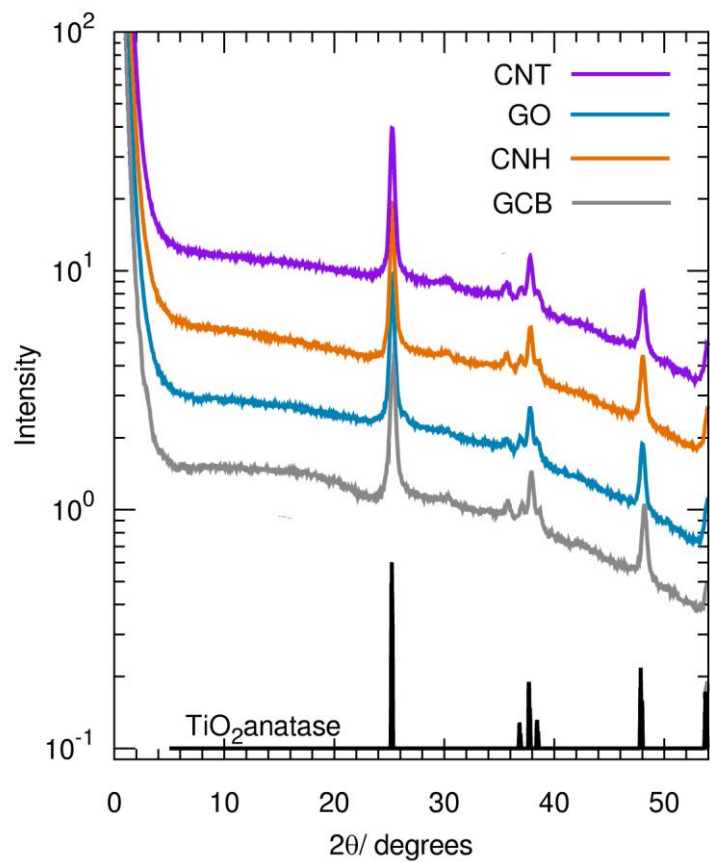


Fig. S8. XRD spectra of the final composites confirmed anatase presence.

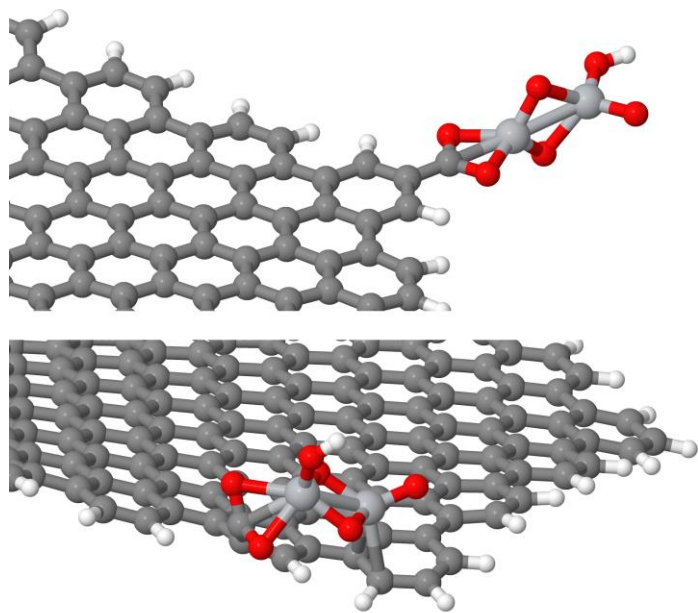


Fig. S9. G-COOH and $(\text{TiO}_2)_2$ binding modes: more stable (top) and less stable (bottom).

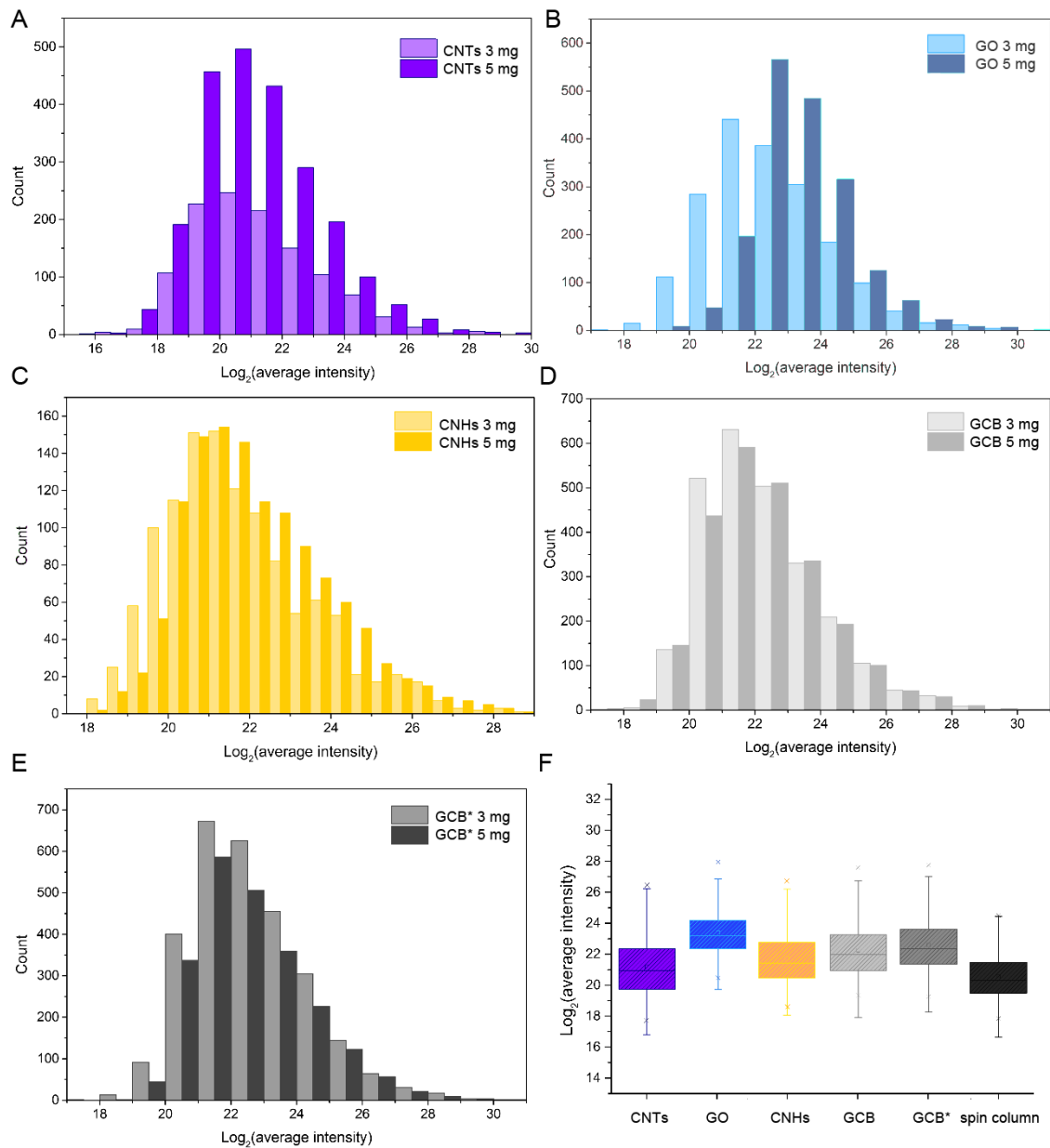


Fig. S10. $\text{Log}_2(\text{average intensity})$ of the phosphopeptides identified with nanocomposites based on A) CNTs, B) GO, C) CNHs, D) GCB, E) GCB with low-level of oxidation (GCB*). F) Box plot of the log_2 (average intensity).

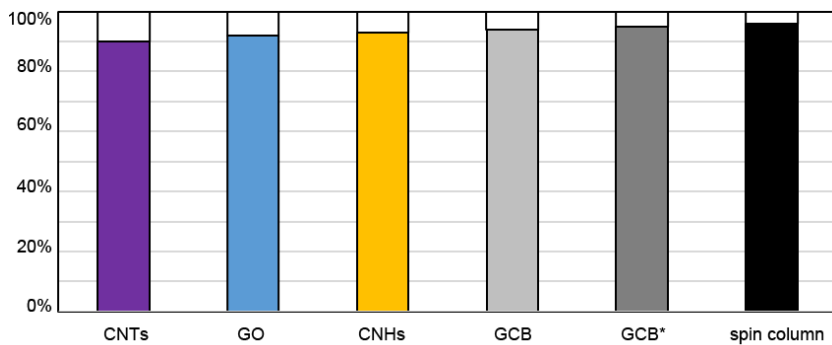


Fig. S11. A negative GRAVY index was found for the vast majority of identified peptides.